Comparing the compression behavior of the antiperovskites CePt$_3$Si, CePt$_3$B, and YPt$_3$B from combined X-ray diffraction experiments and density functional theory

Emma Ehrenreich-Petersen [a], Morten B. Nielsen [a,b], Davide Ceresoli [c], Martin Ottesen [a], Paraskevas Parisiades [d], Martin Bremholm [a,*]

[a] *Department of Chemistry and iNANO, Aarhus University, Langelandsgade 140, Aarhus C 8000, Denmark*
[b] *Danish Technological Institute, Kongsvang Allé 29, Aarhus C 8000, Denmark*
[c] *Consiglio Nazionale delle Ricerche - Istituto di Scienze e Tecnologie Chimiche "G. Natta" (CNR-SCITEC), via Golgi 19, Milano 20133, Italy*
[d] *Sorbonne Université, Institut de Minéralogie, de Physique des Matériaux et de Cosmochimie, CNRS/MNHN/IRD (UMR 7590), 4 Place Jussieu, Paris 75005, France*

ARTICLE INFO

ABSTRACT

In this study we report the synthesis three antiperovskites YPt$_3$B, CePt$_3$B, and CePt$_3$Si as well a focused investigation of YPt$_3$B, which all have the same *P4mm* symmetry with a large c/a ratio at ambient conditions. The compounds are investigated under high-pressure using powder X-ray diffraction in diamond anvil cells. A structural transition is found to occur in the YPt$_3$B compound at 23(2) GPa caused by the softening of a zone boundary phonon. Using a combination of symmetry analysis and structural prediction, the high-pressure phase is assigned to a structure described by the *P*2 (*P*121) space group. Calculation of the phonon dispersion confirms that this structure is dynamically stable with A = Ce, Y and Z = Si, B. It was found that the three APt$_3$Z compounds behave differently with pressure. The bulk moduli for the three compounds are found to be 185(5) GPa, 155(3) GPa, and 128(2) GPa for YPt$_3$B, CePt$_3$B, and CePt$_3$Si, respectively. We found that the Z atom moves away from the center with pressure for A = Ce along the c-axis, whereas for A = Y, the Z atom stays in the approximately same position. This behavior is also reflected in their c/a ratio which stays approximately constant in YPt$_3$B. Overall we find that the Ce-bearing compounds are more compressible in the ab-plane, reducing the tilting of the octahedra. As a result, in YPt$_3$B and CePt$_3$B the transition to the structure described by the *P*2 space group is likely to occur at higher pressures.

1. Introduction

Antiperovskites, a less explored class of materials compared to their perovskite counterparts, exhibit a vast range of interesting properties e. g. giant magnetoresistance [1], negative or zero thermal expansion [2, 3], spin-glass behavior[4], Dirac states close to the Fermi level [5], and superconductivity [6–9–12,13].

In this work we focus on the synthesis and compression behavior of APt$_3$Z antiperovskites, with A = Ce, Y and Z = Si, B. Among these compounds CePt$_3$Si is perhaps the most well-known since it was the first heavy fermion superconductor without a center of symmetry [14]. The low pressure crystal structure of CePt$_3$B is a tetragonally distorted version of the cubic (anti)-perovskite structure with a large c/a ratio of $\simeq 1.34$. The structure is shown in Fig. 1. Here, the atomic positions are

Ce at 1a (0, 0, 0 (z fixed)), Pt1 at 2c (0, 0.5, 0.5134(10)), Pt2 at 1b (0.5, 0.5, 0.1201(11)), and B at 1b (0.5, 0.5, 0.68(3)) [15]. That is, the B atom is displaced away from the center and reside in a tetragonal pyramid formed by five Pt atoms. At low temperatures CePt$_3$B displays two magnetic transitions: a paramagnetic to antiferromagnetic transition at 7.8 K and the appearance of FM ordering at $\approx$ 6 K [16,17].

Other compounds with this structure type include APt$_3$Si (A = La, Pr, Nd, Sm, Gd), and the APt$_3$B (A = La–Nd, Sm, Gd–Tm), although the borides with the heavier rare-earth elements contain an additional cubic phase [18,19]. In addition, using first-principles Yao et al. predicted that the borides and carbides of AT_3Z (A = Sc, Y, La, and T = Pt, Pd and Z = B, C) crystallize in the same structure [20]. In that study, it was found that all compounds were mechanically stable except for ScPt$_3$Z and ScPd$_3$Z. In addition, the bulk moduli were calculated for all mechanically stable

* Corresponding author.
E-mail addresses: davide.ceresoli@cnr.it (D. Ceresoli), bremholm@chem.au.dk (M. Bremholm).
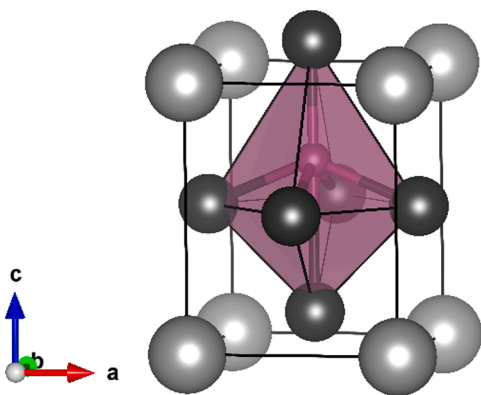
Fig. 1. Crystal structure of $CePt_3B$ in the non-centrosymmetric space group *P4mm* (structural parameters from Ref. [15]). This structure, described by the *P4mm* space group, is the prototype of YPt_3B and $CePt_3Si$. Grey is Ce or Y, black is Pt, and pink is B or Si.

compounds and were found to be in the range from 137 GPa to 191 GPa for each compound. All compounds exhibit metallic behavior and the pressure evolution of the elastic constants showed that the Born-Huang stability criterion is satisfied for YPt_3B and $LaPt_3Z$ up to 40 GPa, the maximum pressure considered in the study [20].

The theoretically proposed compounds YPt_3B, YPd_3B, and $ScPt_3B$ are in addition found to be topological (semi-)metals through a search based on symmetry indicators [21]. Including the antiperovskite counterpart, the perovskites, the structures can be divided into two groups depending on their tetragonality, that is, their c/a ratio. For $BaTiO_3$ [22] and $PbTiO_3$ [23] this ratio is approaching one, whereas for $BiCoO_3$ and $PbVO_3$ the ratio lies between 1.23 and 1.27 [24–26]. This high degree of tetragonality is also observed in the antiperovskites with the $CePt_3B$ structure except for the APd_3C (A = Sc, Y, La) [20].

In the perovskite family, the pressure dependence on the crystal structures are well-studied. It has been found that for $PbVO_3$ a transition to the cubic perovskite at pressures of 2–3 GPa is associated with a large volume drop [25,27]. A transition to cubic structure has also been observed in $BaTiO_3$ around 2 GPa [28] and possibly in $PbTiO_3$ at 11–12 GPa [29–31]. In contrast, $BiCoO_3$ has a structural phase transition at 3 GPa to an orthorhombic (*Pbnm*) structure with an associated spin-state transition [32].

Differently from oxide perovskites, it is conceivable that the large Z atom displacement and large c/a ratio will favor non-centrosymmetric structures even at high pressure. For the APt_3Z antiperovskites in the *P4mm* structure with A = Ce, Y and Z = Si, B, the literature under high pressure is scarce. However, $GdPt_3B$ and $HoPt_3B$ have been investigated and the tetragonal lattices were found to persist up to 20 GPa. In the light of this, we synthesized three antiperovskites, $CePt_3B$ and $CePt_3Si$ and the novel YPt_3B, the latter independently discovered recently as a secondary phase [33], and investigated the structural differences that occur with pressure when changing the rare earth A site from Ce to Y. Thus, the compression behavior of these compounds is extremely important and is the first step towards understanding the evolution of the metallic or superconducting state in non-centrosymmetric compounds.

2. Methods

2.1. Synthesis and high pressure experiments

The samples were made by arc-melting of the elements in an Ar atmosphere and a Zr pellet acted as an oxygen getter to prevent oxidation. All compounds were phase pure except for the $CePt_3B$ where a minor impurity and $CePt_2B$ (space group $P6_222$) were present. High-pressure powder X-ray diffraction (PXRD) experiments using diamond anvil

cells (DAC) were conducted at ID27 at the European Synchrotron Radiation Facility (ESRF). The high-pressure PXRD experiments were done in LeToullec DACs with He as the pressure-transmitting medium. A steel gasket was used for the experiment on $CePt_3B$, whereas Re gaskets were used for $CePt_3Si$ and YPt_3B. A rotation of the DAC was applied during the measurements to improve powder diffraction statistics: from $-3°$ to $+3°$ for $CePt_3B$ during a 10 s exposure time, $-2°$ to $+2°$ for $CePt_3Si$ during 20 s exposure time (increased to 40 s at higher pressures) and $-7°$ to $+7°$ for YPt_3B during 5 s exposure. The wavelength during the experiments was 0.3738 Å and the detector geometry was calibrated with a CeO_2 standard. The pressure was determined from measuring the diffraction signal of a Au piece before and after the sample with the parameters from Ref. [34] The diffraction patterns are modelled using the FullProf Suite[35] using the Le Bail model unless otherwise specified. The main peaks of the $CePt_2B$ impurity are modelled by the Rietveld method. In this paper, the uncertainties on unit cell parameters are from the fitting procedure.

The resulting volumes are fitted with the 3rd order Birch-Murnaghan equation of state (EoS) [36] using the EoSFIT7c program [37]. Structure models are drawn using VESTA [38].

2.2. DFT calculations

The USPEX code [39–41] was used to search for the structures of YPt_3B with the lowest enthalpy at 40 GPa using an evolutionary algorithm. The simulation cell comprised of four formula units. The first generation consisting of 20 structures was generated randomly, and 70% of its low-energy structures were passed on to the next generation. The process was terminated after 40 generations. Each structure relaxation was performed with the VASP code [42] using the PBE functional [43]. The energy and forces were converged to be less than 10^{-4} eV and 0.01 eV/Å, respectively. These DFT calculations were performed with a plane wave energy cutoff of 400 eV and a maximum k-point resolution of $2\pi \cdot 0.06$ Å^{-1}.

The lowest enthalpy structures (i.e. those with *P4mmm* and *P2* symmetry) were selected for DFT calculations to obtain the theoretical equation of state and changes in the structural parameters as a function of pressure. This was performed for the three antiperovskites and included full relaxation of coordinates and cell parameters using Quantum Espresso [44,45]. We used a plane wave cutoff of 50 Ry with ultrasoft pseudopotentials from the GBRV library [46] and the Ce pseudopotential from Ref. [47] and a k-point mesh of $6 \times 6 \times 6$. We used the PBEsol functional [48] because it predicts the equation of state of several systems in fairly good agreement with experiments (for instance see Ref. [49]).

In our calculations, we found that the structure described by the *P2* space group relaxes back to the *P4mm* structure at low pressures, unless the initial coordinates are displaced by more than 0.15 Å from the ideal centrosymmetric perovskite structure. Therefore, we started from 100 GPa – where the structure described by the *P2* space group is more stable than the *P4mm* one – and decreased the pressure in order to obtain the lattice parameters and Wyckoff parameters of both structures. Finally, we investigated the dynamical stability of the structure by computing the phonon dispersion as a function of pressure, using the Density Functional Perturbation Theory [50] implemented in Quantum Espresso.

3. Results and discussion

High pressure powder X-ray diffraction patterns on the three compounds YPt_3B, $CePt_3B$, and $CePt_3Si$ were obtained. Here, the diffraction patterns of YPt_3B confirms that it crystallizes in the *P4mm* space group with the $CePt_3B$ structure (see Fig. 1 for the structure) with a c/a ratio of 1.26 in accordance with [33]. The Rietveld and Le Bail fits are shown in Figure S1 and Figure S2 in the Supporting Information (SI).

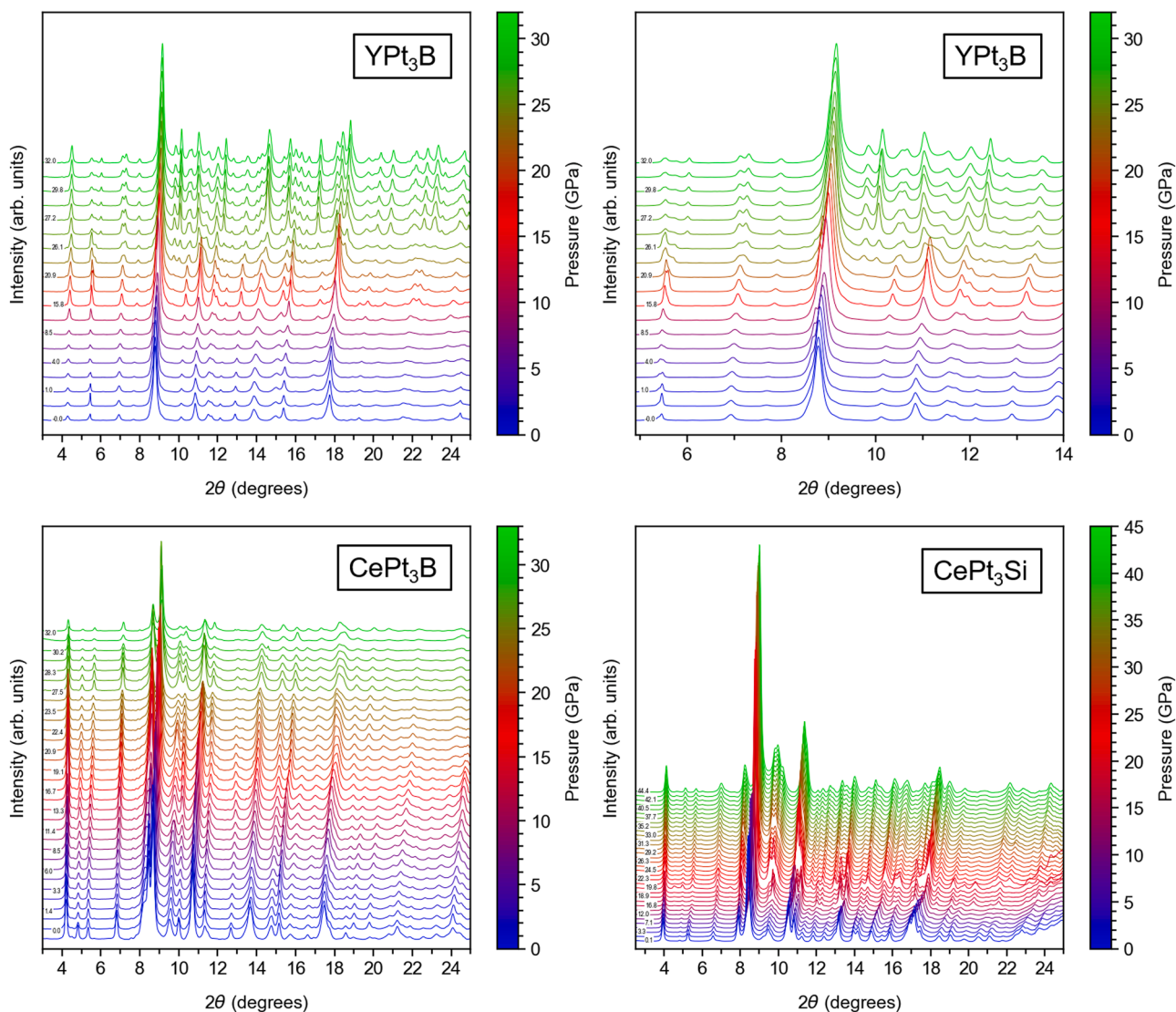The diffraction patterns acquired during compression of YPt_3B (see

Fig. 2. Waterfall plots of the compression of (a) YPt$_3$B and (b) a zoom of the low-angle region of YPt$_3$B, (c) selected diffractograms of CePt$_3$B. The peaks at 8.3° and 9.5° stem from CePt$_2$B, whereas the peak at 4.8° is from an unknown impurity, (d) CePt$_3$Si. The pressure is stated for every second diffraction pattern and is in units of GPa.

Fig. 2a and b) reveal a structural phase transition occurring between 20.92(5) GPa and 23.45(4) GPa, the latter pressure point having the first signs of the new phase as is visible by the appearance of new peaks and the splitting of some peaks. Here, the peak splitting is most pronounced for (101) at 7.1°, (102) at 10.45°, and (200) at 11.2° in 2θ. During decompression, (see Figure S3) a structural transition back to the low-pressure structure is seen at 21.4(1) GPa, which hints towards negligible or no hysteresis for the structural transition and hence a second order phase transition. The maximum pressure reached during the experiment was 32.00(3) GPa. The waterfall plots of the diffractograms obtained during compression of the isostructural antiperovskites CePt$_3$B (max. pressure: 32.04(15) GPa, Fig. 2c) and CePt$_3$Si (max. pressure: 44.76(5) GPa, Fig. 2d) show no phase transitions in the investigated pressure interval. The only changes in the diffractograms are the movement of the diffraction peaks to higher scattering angle with pressure as is expected from the gradual compression of the unit cell with pressure. For the CePt$_3$B an unidentified impurity as well as CePt$_2$B (space group $P6_2 22$) is present in the diffractogram.

3.1. High-pressure structure of YPt$_3$B

The high pressure phase of YPt$_3$B is discussed first. The DFT calculations of the dynamical stability of the *P4mm* structure, shown in Fig. 3, reveals a structural phase transition due to a phonon instability at the M point of the Brillouin zone at about 20 GPa, which is in good agreement with the experimental data. The instability corresponds to the mode displayed in Figure S9 for which the unit cell volume doubles and apical Pt atoms approach each other in pairs along the *b*-axis. For the sake of completeness, the full phonon dispersion is shown in Figure S7.

As shown in Figure S4, the texture in the PXRD data becomes severe when approaching the structural phase transition, thereby limiting the reliability of Rietveld refinements. Therefore, our strategy to solve the high pressure structure of YPt$_3$B was based on combining crystal structure predictions using USPEX [39–41] with group-subgroup relationships.

If we assume that the phase transition is of second order it requires a direct group-subgroup relationship between the initial and final structures. Therefore, the space group of the high pressure phase is a subgroup of *P4mm*. Since peak splitting is observed, it is unlikely that the 4-fold rotation axis will be retained in the subgroup. This limits the choice
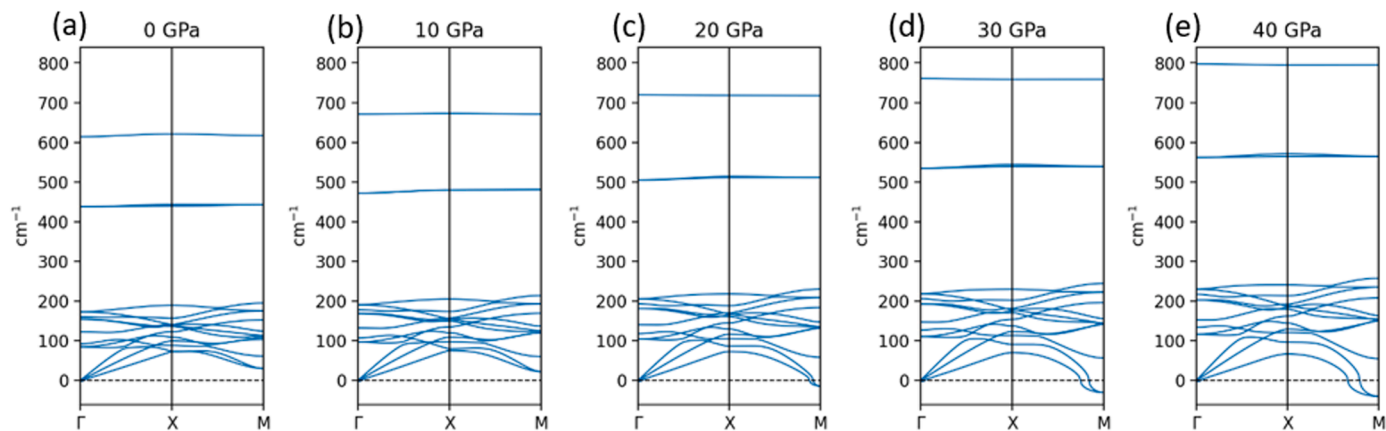
Fig. 3. Phonon dispersion for the *P4mm* phase of YPt$_3$B at (a) 0 GPa, (b) 10 GPa, (c) 20 GPa and (d) 30 GPa, and (e) 40 GPa.

of possible subgroups to the two members of the *mm*2 point group (*Pmm*2 and *Cmm*2). This is shown in the first step of the symmetry reduction tree presented in Fig. 4a. The *translationengleiche* subgroups of these space groups are given in Fig. 4a, which goes all the way down to the *P*1 space group.

If, on the other hand, there is no assumption that it necessarily is a second-order phase transition, USPEX can be utilized. Here, the USPEX search for possible high pressure structures was performed on four formula units in the simulation cell and at 40 GPa. The ID number, enthalpy, and space group is given in Table S1 for the 8 structures with the lowest enthalpy. Inspecting the USPEX results, one structure has a significantly lower enthalpy compared to the others (0.0698 eV/atom), namely the structure described by the *P*2 space group. This space group also appears from the symmetry analysis. The unit cell contains two formula units whereas the low pressure (*P4mm*) cell contains only one. To achieve a unit cell consistent with that through symmetry reductions, there is only one way, namely: *P4mm* ⟶ *Cmm*2 ⟶ *Pmm* ⟶ *P*2, since the path that starts by going from *P4mm* to *Pmm*2 or directly from *Cmm*2 to *P*2 only contains one formula unit. The Bärnighausen tree of the symmetry reduction path is shown in Figure S6 and the structure described by the *P*2 space group is shown in Fig. 4b.

In the first step from *P4mm* to *Cmm*2, the volume of the unit cell is doubled by multiplying $\sqrt{2}$ to both the *a*- and *b*-axis. In the next step from *Cmm*2 to *Pmm*2, the atomic sites split into several symmetry independent sites. A further split in atomic sites are achieved going from *Pmm*2 to *P*2, while the unit cell axes are permuted (*a* to *c*, *b* to *a*, and *c* to *b*). A comparison of the unit cell parameters is shown in Table 1. This is done for the unit cell deduced from symmetry considerations obtained for the highest pressure where the *P4mm* structure is stable and

Table 1

Comparison of the unit cell parameters deduced from the last pressure point in which the *P4mm* structure is stable (∼ 20 GPa) and that of the USPEX unit cell (40 GPa).

	a (Å)	*b* (Å)	*c* (Å)	*β* (°)
*P*2	5.4302(2)	4.8362(5)	5.4302(2)	90
USPEX	5.347	4.802	5.359	90.21

computationally through an USPEX search. Here, an excellent fit exists between the two procedures when keeping in mind that the USPEX search is performed at 40 GPa whereas the pressure is derived from ∼ 20 GPa, which explains the slightly lower unit cell parameters from the USPEX search.

To confirm the predicted structural model (see Fig. 4b) after the phase transition, a refined diffractogram with the *P*2 space group is shown in Fig. 5 using Le Bail fits. The Rietveld refinement is shown in Figure S5 with the atomic positions derived from the symmetry analysis.

To explore the thermodynamical relationship between the low pressure and high pressure phases of YPt$_3$B, we calculated the enthalpy of the two different phases. The result of this is shown in Fig. 6. Here, it is seen that the enthalpies among the different phases remains degenerate within the numerical accuracy up to pressures around 25 GPa. From here on, the *P*2 symmetry becomes increasingly more favorable compared to the *P4mm* symmetry in good agreement with the experimental results. It should be noted that below 20 GPa, the structural difference between the two phases is minimal, since the monoclinic angle (*β*) is very close to 90 degrees for the structure described by the *P*2 space group after which it quickly increases with increasing pressure
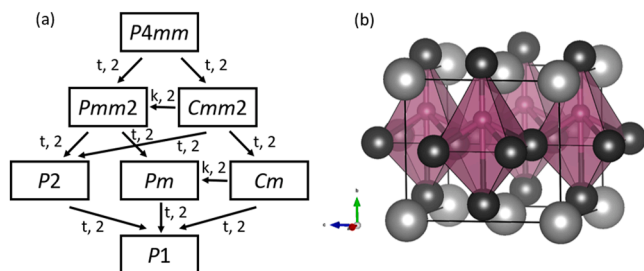

Fig. 4. (a) Maximal subgroups of *P4mm* that break the 4-fold symmetry of the tetragonal cell and changes the space group type. Only the *translationengleiche* subgroups have been included for *Pmm*2 and *Cmm*2. The index and type of symmetry reduction is shown along the arrows of each reduction. (b) The structure described by the *P*2 space group of YPt$_3$B from a symmetry reduction of *P4mm* ⟶ *Cmm*2 ⟶ *Pmm*2 ⟶ *P*2. The grey spheres are Y, the black are Pt, and the purple/red are B.
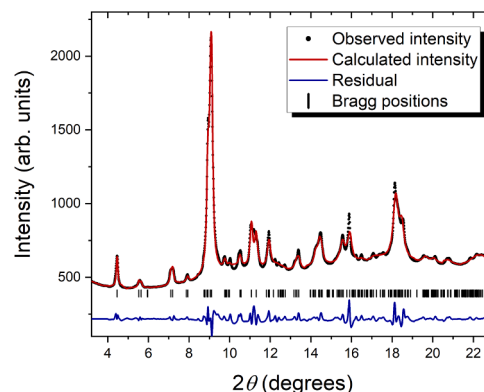

Fig. 5. Le Bail fit of YPt$_3$B after the structural phase transition is completed. The structure model is refined with the *P*2 space group symmetry and *P* = 23.45 (4) GPa.
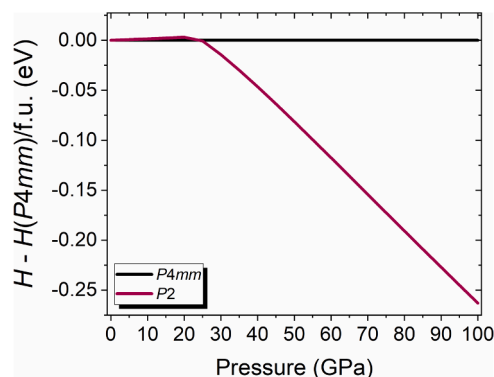
Fig. 6. Relative enthalpy per unit formula of YPt$_3$B as a function of pressure as calculated by DFT. Below 30 GPa the structure described by the *P2* space group becomes identical to the one described by the *P4mm* space group. The small difference (few meV/u.f.) below 30 GPa is the numerical error of the DFT calculation when comparing structures with different unit formulas and different k-point sampling.

(see Fig. 8). To further support that the high pressure phase is the structure described by the *P2* space group, we computed the phonon dispersion of the *P2* phase of YPt$_3$B at 0 and 20 GPa, which confirms that the structure is dynamically stable (see Figure S8).

The thermodynamic relationship among the *P4mm* and structure described by the *P2* space groups has also been investigated for CePt$_3$B and CePt$_3$Si and is reported in Figure S12. Here the enthalpies are degenerate to numerical accuracy (which can be estimated as few meV/ f.u.). This is caused by the fact that the DFT calculations do not support the monoclinic distortion. Instead, we observed that the structures relaxed to the *P4mm* structures in the whole pressure range investigated, suggesting that the structure described by the *P2* space group is not stable up to 100 GPa. This behavior is further confirmed by the absence of unstable phonon modes up to 40 GPa. In fact, as reported in Figure S10 and Figure S11, the phonon dispersions of the *P4mm* phases of CePt$_3$B and CePt$_3$Si show that CePt$_3$Si becomes dynamically unstable at 100 GPa, whereas CePt$_3$B is dynamically stable from 0 GPa up to 100 GPa. A possible explanation for the striking difference with respect to YPt$_3$B might relay in the different compression behavior of the thee materials, as discussed in the following section.

3.2. Pressure evolution of structural parameters

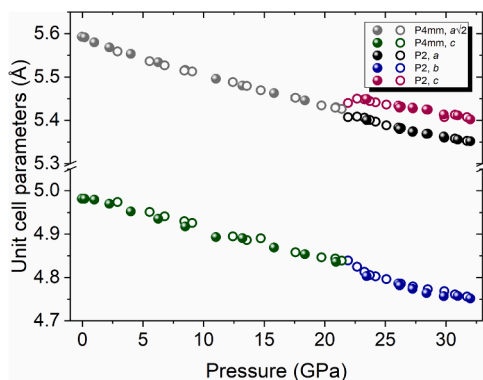The refined unit cell parameters of both the *P4mm* and structure described by the *P2* space group of YPt$_3$B obtained by experiment are shown in Fig. 7. Here, the *a*-axis of the *P4mm* structure has been scaled by $\sqrt{2}$ for a better comparison to the monoclinic *P2* unit cell. It is seen that the *b*-axis of the structure described by the *P2* space group follows the compression behavior of the *c*-axis from the *P4mm* structure. Another thing to notice is a slight splitting of the value of the *a*- and *c*-axis from what is expected from the compression of the *P4mm*.

The monoclinic angle β is shown in Fig. 8 as calculated by DFT and from the experimental compression and decompression experiments. The DFT calculated angle is displaced only very slightly to lower pressures compared to experiments. In addition, it appears from both DFT and experiment that the monoclinic angle is rapidly diverging from 90° near 20 GPa and is increasing with increasing pressure before an apparent plateau at higher pressures. This implies that the order parameter of the second order phase transition can be related to the monoclinic angle. In general, in a ferroelastic phase transition, the correct order parameter is the *spontaneous scalar strain* ϵ. We calculated the spontaneous strain components and we reported them in Sec. 6 of the SI, following a procedure similar to Ref. [51]. In this particular case, the spontaneous strain component ϵ_{31} is the dominant contribution, and as shown in Fig. S15, its evolution with pressure is very similar to that of the monoclinic angle. Therefore, the monoclinic angle is a clear indicator of the nature of the phase transition. The order parameter, η, is given by: $\eta(P) = A|\frac{P_c-P}{P_c}|^\alpha$, where P_c is the critical pressure of the phase transition, α is the critical exponent and A is a constant. Therefore, we fitted this equation to the DFT data points in Fig. 8, whereas the fits from experiments are shown in Figure S14. The fitting parameters are given in Table 2. In all cases, the fitting interval is chosen as the first point where the monoclinic angle deviates significantly from 90°. The predicted critical pressures suggest a phase transition slightly above 23 GPa, whereas it is less than 22 GPa during decompression where the pressure sampling close to the phase transition is better.

The unit cell parameters as a function of pressure is seen in Fig. 9a for the *P4mm* structures, whereas the *c/a* ratio is shown in Fig. 9b, all from experiments. The same plot with DFT results are shown in Figure S13. The results show that DFT slightly overestimates the *c/a* ratio for all three compounds, although the overall behavior is similar for YPt$_3$B and CePt$_3$Si.

The rather peculiar pressure evolution of the *c/a* ratio, as shown in Fig. 9b, of CePt$_3$B might be ascribed to the presence of additional phases in the diffractogram or from the presence of strain in the sample. However, looking closely at the DFT results, the *c/a* ratio is constant up to 10 GPa, after which it increases with pressure. Therefore, the behavior obtained from experiment – although it is more pronounced – might be a real feature. Fig. 9a reveals that the cause of the rapid
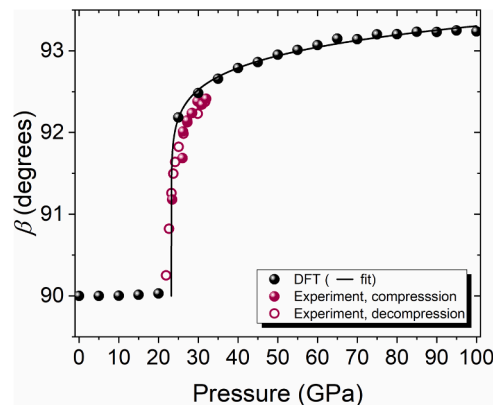

Fig. 7. The refined unit cell parameters for YPt$_3$B in both the low pressure (*P4mm*) phase and the high pressure (*P2*) phase during the compression and decompression. The filled symbols are from the compression experiment, whereas the open circles correspond to results from the decompression experiment.

Fig. 8. The monoclinic angle, β, from the structure described by the *P2* space group of YPt$_3$B as calculated by DFT and during both compression and decompression experiments. The β angle from DFT is fitted with the equation $\eta(P) = \beta - 90° = A|\frac{P_c-P}{P_c}|^\alpha$.

Table 2
Fitting parameters for the order parameter $\eta(P)$ in the structure described by the $P2$ space group for YPt$_3$B.

Method	A	P_c (GPa)	α
DFT	2.89(5)	23.24(1)	0.111(13)
Expt., compression	3.1(7)	23.1(11)	0.24(18)
Expt., decompression	3.2(3)	21.91(3)	0.32(7)

increase in c/a ratio for CePt$_3$B is due to the fact that the c-axis plateaus. Fig. 9b also reveals two different compression behaviors, namely that the ratio is increasing for CePt$_3$Si and CePt$_3$B, whereas it is nearly constant or even slightly decreasing for YPt$_3$B. This implies that the boron atom moves away from the center for the Ce analogues with pressure, whereas the boron atom moves slightly towards the center for the Y analogue. This behavior is reproduced in DFT calculations and it is shown in Figure S13. Therefore, the difference in compression behavior stems from the different A atoms in the APt$_3$Z compounds and might be related to the presence of $4f$ electrons in the Ce compounds. The vastly different compression behavior is thus a good indication as to why we do not observe structural phase transition in the Ce analogues.

Fig. 10 displays the volume as a function of pressure for all three compounds from both experiments and DFT. The volumes are slightly underestimated by DFT at lower pressures, whereas at higher pressures, the DFT calculated volume and that from experiment are in better agreement. Focusing on the YPt$_3$B compound, it is clear that there is no associated volume drop transitioning from the $P4mm$ to structure described by the $P2$ space group, which again suggests that it is a second order phase transition, where discontinuity is seen in (at least) one of the second derivatives of the Gibbs free energy and not in the volume. Otherwise, the volumes decrease smoothly with pressure as expected.

The volume data in Fig. 10 has been fitted to the 3rd order Birch-Murnaghan EoS and the results are displayed in Fig. 11 for all $P4mm$ structures. The structure described by the $P2$ space group of YPt$_3$B was not fitted due to the limited amount of pressure points. The EoS fits are shown in Figure S16. The covariance plot of K_0' with K_0 is shown in Figure S17. The top panel of Fig. 11 shows the corresponding bulk moduli as a function of the ambient pressure volume. From this, it is clear the bulk modulus increases with increasing volume at ambient pressure. The bulk modulus of YPt$_3$B is in great agreement with the paper by Yao and coauthors [20], who predicted $K_0 = 188$ GPa using DFT. In contrast, the bulk modulus obtained in this work differs significantly from that obtained by experimental procedures by Rogl et al. [52]. Here, the bulk moduli are 103 or 111 and 98 or 105 GPa depending on different loads for the nanoindentation for CePt$_3$Si and CePt$_3$B, respectively, which is lower than the values obtained here. However, they obtain $K_0 = 144$ GPa and 167 GPa for CePt$_3$Si and CePt$_3$B, respectively, using DFT including the Hubbard U correction,
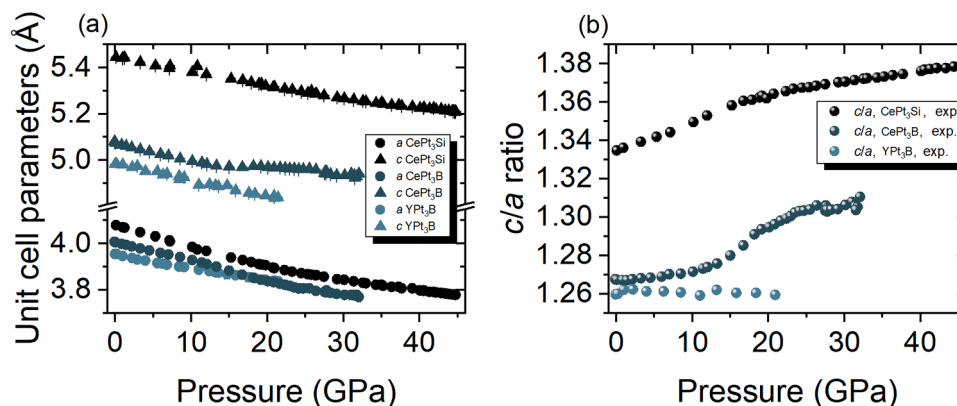
which is close to the values obtained in this work. In addition, a bulk modulus for CePt$_3$Si of 162 GPa is reported by Nicklas et al. referring to unpublished work by Ohashi et al. [53], which is significantly higher than the value reported here. Comparing to the tetragonally-distorted
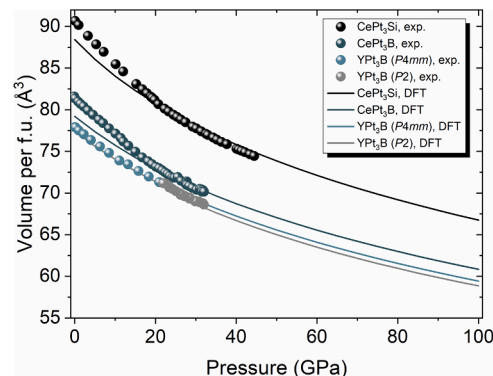

Fig. 10. The volume as a function of pressure for the $P4mm$ phases of CePt$_3$B, CePt$_3$Si, and YPt$_3$B as well as the volume of the $P2$ phase of YPt$_3$B as obtained from both compression experiments (circles) and by DFT (lines).
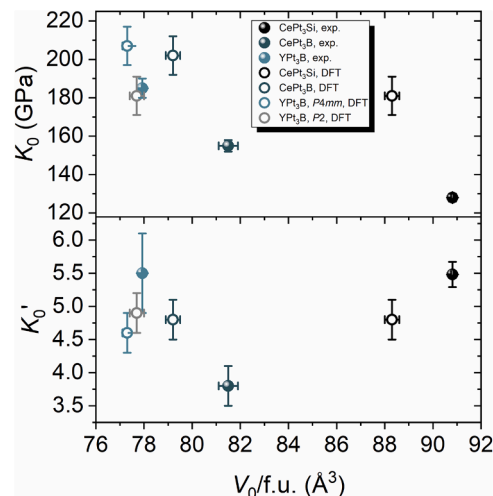

Fig. 11. Results from fitting of the 3rd order Birch-Murnaghan EoS for all $P4mm$ structures. The structure described by the $P2$ space group for YPt$_3$B is not included due to the limited amount of pressure points. The top shows the bulk modulus versus volume at zero pressure and the bottom shows the pressure derivative of the bulk modulus as a function of volume at zero pressure.

Fig. 9. (a) Unit cell parameters as a function of pressure for CePt$_3$B, CePt$_3$Si, and YPt$_3$B. (b) The c/a ratio as a function of pressure for the three compounds CePt$_3$B, CePt$_3$Si, and YPt$_3$B.

perovskite counterparts, the bulk modulus is found to be 61(2) GPa for $PbVO_3$ [27] and 74(3) GPa for $BiCoO_3$ [32]. For the less tetragonally distorted perovskites, the bulk moduli have been found to be $\approx$ 100 GPa [29,54] and 135–179(3) GPa [55,56] for $PbTiO_3$ and $BaTiO_3$, respectively. In addition, the pressure derivative of the bulk modulus is plotted versus V_0 in the bottom panel of Fig. 11. Here, it is noted that all values lie close to $K' = 4$ as is obtained from a second order Birch-Murnaghan fit as is often done in literature [27,29,32,54,56]. However, $BaTiO_3$ is reported with a $K' = 6.4$, which is higher than the ones obtained in this work. The small number of antiperovskite studies published today compared with those of the perovskite suggests that there is a huge gap of novel compounds and properties left to be filled. Therefore, with this study, we want to motivate the discovery and characterization of further antiperovskite compounds.

4. Conclusion

We report for the first time the synthesis of pure YPt_3B, which crystallizes in the same *P4mm* space group as the isostructural compounds $CePt_3B$ and $CePt_3Si$, all with a large degree of tetragonality. The high pressure behavior of the three compounds were investigated by synchrotron high-pressure X-ray diffraction in diamond anvil cells. Here, a phase transition from the *P4mm* to *P2* symmetry occurred above 21 GPa for YPt_3B. The structure of the high-pressure phase was solved through a combination of Crystal Structure Prediction methods and symmetry considerations. The phase transition is shown to be of second order with the monoclinic β angle as the order parameter. From the fit of the order parameter a critical pressure for the phase transition is found around 22–23 GPa. The isostructural compounds $CePt_3B$ and $CePt_3Si$ do not have a structural transition up to the highest pressure in this study; 32 GPa and 45 GPa, respectively. The volumes of the three structures were fitted with the 3rd order Birch-Murnaghan EoS, from which the bulk moduli (K_0) are found to be 185(5) GPa, 155(3) GPa, and 128(2) GPa for YPt_3B, $CePt_3B$, and $CePt_3Si$, respectively. The corresponding pressure derivatives of the bulk moduli (K') are found to be 5.5(6), 3.8 (3), and 5.48(19), respectively. The c/a ratio shows different compression behavior when substituting $A =$ Ce or Y in APt_3Z compounds. That is, the ratio is slightly decreasing with pressure for YPt_3B, whereas it is increasing for $CePt_3B$ and $CePt_3Si$, which is caused by the movement of the B/Si atoms away from the center alng the c-axis in the Ce-bearing compounds. DFT calculations for the three compounds are in very good agreement with the results obtained by the experimental X-ray data and support the structure solution and suggest a second order phase transition as a function of pressure. The larger a, b compressibility of $CePt_3B$ and $CePt_3Si$ depresses the tilting and rotation of the octahedra and as a consequence the transition to the *P2* phase is likely to occur at much higher pressures.

CRediT authorship contribution statement

Martin Bremholm: Writing – review & editing, Validation, Supervision, Project administration, Methodology, Funding acquisition, Data curation, Conceptualization. **Emma Ehrenreich-Petersen:** Writing – review & editing, Writing – original draft, Visualization, Validation, Investigation, Formal analysis. **Davide Ceresoli:** Writing – review & editing, Visualization, Validation, Resources, Methodology, Investigation, Formal analysis. **Morten B. Nielsen:** Writing – review & editing, Methodology, Investigation, Formal analysis, Data curation, Conceptualization. **Paraskevas Parisiades:** Writing – review & editing, Resources, Investigation, Data curation. **Martin Ottesen:** Writing – review & editing, Validation.

Declaration of Competing Interest

The authors declare that they have no known competing financial interests or personal relationships that could have appeared to influence the work reported in this paper.

Data Availability

Data will be made available on request.

Appendix A. Supporting information

Supplementary data associated with this article can be found in the online version at doi:10.1016/j.jallcom.2024.177204.

References

[1] K. Kamishima, T. Goto, H. Nakagawa, N. Miura, M. Ohashi, N. Mori, T. Sasaki, T. Kanomata, Giant magnetoresistance in the intermetallic compound Mn_3 GaC, Phys. Rev. B 63 (2) (2000) 024426, https://doi.org/10.1103/PhysRevB.63.024426.

[2] T. Hamada, K. Takenaka, Giant negative thermal expansion in antiperovskite manganese nitrides, J. Appl. Phys. 109 (7) (2011) 07E309, https://doi.org/10.1063/1.3540604.

[3] K. Takenaka, H. Takagi, Zero thermal expansion in a pure-form antiperovskite manganese nitride, Appl. Phys. Lett. 94 (13) (2009) 131904, https://doi.org/10.1063/1.3110046.

[4] C. Liu, X. Tao, X. Kan, X. Liu, C. Zhang, S. Feng, Y. Yang, Q. Lv, J. Hu, M. Shezad, Spin-glass behavior in Co-based antiperovskite compound $SnNCo_3$, Appl. Phys. Lett. 116 (5) (2020) 052401, https://doi.org/10.1063/1.5140434.

[5] A. Pertsova, R.M. Geilhufe, M. Bremholm, A.V. Balatsky, Computational search for dirac and weyl nodes in *f*-electron antiperovskites, Phys. Rev. B 99 (2019) 205126, https://doi.org/10.1103/PhysRevB.99.205126.

[6] T. He, Q. Huang, A.P. Ramirez, Y. Wang, K.A. Regan, N. Rogado, M.A. Hayward, M. K. Haas, J.S. Slusky, K. Inumara, H.W. Zandbergen, N.P. Ong, R.J. Cava, Superconductivity in the non-oxide perovskite $MgCNi_3$, Nature 411 (6833) (2001) 54, https://doi.org/10.1038/35075014.

[7] A. Iyo, I. Hase, H. Fujihisa, Y. Gotoh, S. Ishida, H. Ninomiya, Y. Yoshida, H. Eisaki, H.T. Hirose, T. Terashima, K. Kawashima, Antiperovskite superconductor $LaPd_3P$ with noncentrosymmetric cubic structure, Inorg. Chem. 60 (23) (2021) 18017, https://doi.org/10.1021/acs.inorgchem.1c02604.

[8] M. Oudah, A. Ikeda, J.N. Hausmann, S. Yonezawa, T. Fukumoto, S. Kobayashi, M. Sato, Y. Maeno, Superconductivity in the antiperovskite dirac-metal oxide $Sr_{3−x}SnO$, Nat. Commun. 7 (1) (2016) 13617, https://doi.org/10.1038/ncomms13617.

[9] T. Takayama, K. Kuwano, D. Hirai, Y. Katsura, A. Yamamoto, H. Takagi, Strong coupling superconductivity at 8.4 K in an antiperovskite phosphide $SrPt_3P$, Phys. Rev. Lett. 108 (23) (2012) 237001, https://doi.org/10.1103/PhysRevLett.108.237001.

[10] M. Uehara, A. Uehara, K. Kozawa, T. Yamazaki, Y. Kimishima, New antiperovskite superconductor $ZnNNi_3$, and related compounds $CdNNi_3$ and $InNNi_3$, Phys. C. Supercond. 470 (2010) S688, https://doi.org/10.1016/j.physc.2009.11.131.

[11] B. He, C. Dong, L. Yang, X. Chen, L. Ge, L. Mu, Y. Shi, $CuNNi_3$: a new nitride superconductor with antiperovskite structure, Supercond. Sci. Technol. 26 (12) (2013) 125015, https://doi.org/10.1088/0953-2048/26/12/125015.

[12] M. Uehara, T. Yamazaki, T. Kōri, T. Kashida, Y. Kimishima, I. Hase, Superconducting properties of $CdCNi_3$, J. Phys. Soc. Jpn. 76 (3) (2007) 034714, https://doi.org/10.1143/JPSJ.76.034714.

[13] M. Uehara, A. Uehara, K. Kozawa, Y. Kimishima, New antiperovskite-type superconductor ZnN_yNi_3, J. Phys. Soc. Jpn. 78 (3) (2009) 033702, https://doi.org/10.1143/jpsj.78.033702.

[14] E. Bauer, G. Hilscher, H. Michor, C. Paul, E.W. Scheidt, A. Gribanov, Y. Seropegin, H. Noël, M. Sigrist, P. Rogl, Heavy fermion superconductivity and magnetic order in noncentrosymmetric $CePt_3Si$, Phys. Rev. Lett. 92 (2) (2004) 027003, https://doi.org/10.1103/PhysRevLett.92.027003.

[15] O.L. Sologub, J.R. Hester, P.S. Salamakha, E. Leroy, C. Godart, Ab initio structure determination of new boride $CePt_3B$, a distorted variant of $CaTiO_3$, J. Alloy. Compd. 337 (1) (2002) 10, https://doi.org/10.1016/S0925-8388(01)01913-2.

[16] D. Rauch, S. Süllow, M. Bleckmann, A. Buchsteiner, N. Stüßer, H.H. Klauss, H. Luetkens, E. Bauer, Magnetic order in non-centrosymmetric CePt$_3$B, J. Phys. Conf. Ser. 391 (2012) 012055, https://doi.org/10.1088/1742-6596/391/1/012055.

[17] S. Süllow, G.J. Nieuwenhuys, A.A. Menovsky, J.A. Mydosh, Unusual magnetic behavior of CePt$_3$B, Phys. B Condens. Matter 199-200 (1994) 644, https://doi.org/10.1016/0921-4526(94)91933-X.

[18] S. Mondal, C. Mazumdar, R. Ranganathan, M. Avdeev, Structural transformation in inverse-perovskite REPt$_3$B (RE = Sm and Gd-Tm) associated with large volume reduction, Inorg. Chem. 56 (14) (2017) 8446, https://doi.org/10.1021/acs.inorgchem.7b01131.

[19] O.L. Sologub, K. Hiebl, P.S. Salamakha, H. Ipser, Crystal structure and physical properties of ternary compounds RPt$_3$B, R = La, Pr, Nd, J. Alloy. Compd. 360 (1) (2003) 54, https://doi.org/10.1016/S0925-8388(03)00373-6.

[20] T. Yao, Y. Wang, H. Li, J. Lian, J. Zhang, H. Gou, First-principles study of structural stability, elastic and electronic properties of ternary rare earth-transition metal—borides and carbides RT$_x$S, R = Sc, Y, and La, T = Pt and Pd, Z = B and C, and x = 2, 3, and 4), Phys. B Condens. Matter 431 (2013) 58, https://doi.org/10.1016/j.physb.2013.08.031.

[21] F. Tang, H.C. Po, A. Vishwanath, X. Wan, Comprehensive search for topological materials using symmetry indicators, Nature 566 (7745) (2019) 486, https://doi.org/10.1038/s41586-019-0937-5.

[22] H.D. Megaw, Crystal structure of barium titanate, Nature 155 (3938) (1945) 484, https://doi.org/10.1038/155484b0.

[23] S.V. Náray-Szabó, Die strukturen von verbindungen ABO$_3$ "Schwesterstrukturen, Sci. Nat. 31 (39) (1943) 466, https://doi.org/10.1007/BF01468312.

[24] R.V. Shpanchenko, V.V. Chernaya, A.A. Tsirlin, P.S. Chizhov, D.E. Sklovsky, E.V. Antipov, E.P. Khlyov, V. Pomjakushin, A.M. Balagurov, J.E. Medvedeva, E.E. Kaul, C. Geibel, Synthesis, structure, and properties of new perovskite PbVO$_3$, Chem. Mater. 16 (17) (2004) 3267, https://doi.org/10.1021/cm049310x.

[25] A.A. Belik, M. Azuma, T. Saito, Y. Shimakawa, M. Takano, Crystallographic features and tetragonal phase stability of PbVO$_3$, a new member of PbTiO$_3$ family, Chem. Mater. 17 (2) (2005) 269–273, https://doi.org/10.1021/cm048387i.

[26] A.A. Belik, S. Iikubo, K. Kodama, N. Igawa, S. Shamoto, S. Niitaka, M. Azuma, Y. Shimakawa, M. Takano, F. Izumi, E. Takayama-Muromachi, Neutron powder diffraction study on the crystal and magnetic structures of BiCoO$_3$, Chem. Mater. 18 (3) (2006) 798–803, https://doi.org/10.1021/cm052334z.

[27] W. Zhou, D. Tan, W. Xiao, M. Song, M. Chen, X. Xiong, J. Xu, Structural properties of PbVO$_3$ perovskites under hydrostatic pressure conditions up to 10.6 GPa, J. Phys. Condens. Matter 24 (43) (2012) 435403, https://doi.org/10.1088/0953-8984/24/43/435403.

[28] U.D. Venkateswaran, V.M. Naik, R. Naik, High-pressure raman studies of polycrystalline BaTiO$_3$, Phys. Rev. B 58 (21) (1998) 14256–14260, https://doi.org/10.1103/PhysRevB.58.14256.

[29] A. Sani, M. Hanfland, D. Levy, The equation of state of PbTiO$_3$ up to 37 GPa: a synchrotron x-ray powder diffraction study, J. Phys. Condens. Matter 14 (44) (2002) 10601–10604, https://doi.org/10.1088/0953-8984/14/44/340.

[30] J.A. Sanjurjo, E. López-Cruz, G. Burns, Pressure dependence of the linewidth of the soft phonons in PbTiO$_3$, Solid State Commun. 48 (3) (1983) 221–224, https://doi.org/10.1016/0038-1098(83)90274-0.

[31] P.E. Janolin, P. Bouvier, J. Kreisel, P.A. Thomas, I.A. Kornev, L. Bellaiche, W. Crichton, M. Hanfland, B. Dkhil, High-pressure effect on PbTiO$_3$: An investigation by raman and x-ray scattering up to 63 GPa, Phys. Rev. Lett. 101 (23) (2008) 237601, https://doi.org/10.1103/PhysRevLett.101.237601.

[32] K. Oka, M. Azuma, W. Chen, H. Yusa, A.A. Belik, E. Takayama-Muromachi, M. Mizumaki, N. Ishimatsu, N. Hiraoka, M. Tsujimoto, M.G. Tucker, J.P. Attfield, Y. Shimakawa, Pressure-induced spin-state transition in BiCoO$_3$, J. Am. Chem. Soc. 132 (27) (2010) 9438, https://doi.org/10.1021/ja102987d.

[33] L. Salamakha, O. Sologub, B. Stöger, G. Giester, P.F. Rogl, H. Michor, E. Bauer, Electronic and structural properties of mptxb6-2x (m = y, yb): Structural disorder in an octahedral boron framework, pMID: 37948347, Inorg. Chem. 62 (47) (2023) 19164–19177, https://doi.org/10.1021/acs.inorgchem.3c01526.

[34] Y. Fei, A. Ricolleau, M. Frank, K. Mibe, G. Shen, V. Prakapenka, Toward an internally consistent pressure scale, Proc. Natl. Acad. Sci. 104 (22) (2007) 9182–9186, https://doi.org/10.1073/pnas.0609013104.

[35] J. Rodríguez-Carvajal, Recent advances in magnetic structure determination by neutron powder diffraction, Phys. B Condens. Matter 192 (1) (1993) 55, https://doi.org/10.1016/0921-4526(93)90108-I.

[36] F. Birch, Finite elastic strain of cubic crystals, Phys. Rev. 71 (1947) 809, https://doi.org/10.1103/PhysRev.71.809.

[37] R.J. Angel, M. Alvaro, J. Gonzalez-Platas, Eosfit7c and a fortran module (library) for equation of state calculations, Z. Krist. - Cryst. Mater. 229 (5) (2014) 405–419, https://doi.org/10.1515/zkri-2013-1711.

[38] K. Momma, F. Izumi, *VESTA3* for three-dimensional visualization of crystal, volumetric and morphology data, J. Appl. Crystallogr. 44 (6) (2011) 1272, https://doi.org/10.1107/S0021889811038970.

[39] A.R. Oganov, C.W. Glass, Crystal structure prediction using ab initio evolutionary techniques: Principles and applications, J. Chem. Phys. 124 (24) (2006) 244704, https://doi.org/10.1063/1.2210932.

[40] A.R. Oganov, A.O. Lyakhov, M. Valle, How evolutionary crystal structure prediction works—and why, Acc. Chem. Res. 44 (3) (2011) 227–237, https://doi.org/10.1021/ar1001318.

[41] A.O. Lyakhov, A.R. Oganov, H.T. Stokes, Q. Zhu, New developments in evolutionary structure prediction algorithm USPEX, Comput. Phys. Commun. 184 (4) (2013) 1172, https://doi.org/10.1016/j.cpc.2012.12.009.

[42] G. Kresse, J. Furthmüller, Efficient iterative schemes for ab initio total-energy calculations using a plane-wave basis set, Phys. Rev. B 54 (1996) 11169, https://doi.org/10.1103/PhysRevB.54.11169.

[43] J.P. Perdew, K. Burke, M. Ernzerhof, Generalized gradient approximation made simple, Phys. Rev. Lett. 77 (1996) 3865–3868, https://doi.org/10.1103/PhysRevLett.77.3865.

[44] P. Giannozzi, S. Baroni, N. Bonini, M. Calandra, R. Car, C. Cavazzoni, D. Ceresoli, G.L. Chiarotti, M. Cococcioni, I. Dabo, A.D. Corso, S. de Gironcoli, S. Fabris, G. Fratesi, R. Gebauer, U. Gerstmann, C. Gougoussis, A. Kokalj, M. Lazzeri, L. Martin-Samos, N. Marzari, F. Mauri, R. Mazzarello, S. Paolini, A. Pasquarello, L. Paulatto, C. Sbraccia, S. Scandolo, G. Sclauzero, A.P. Seitsonen, A. Smogunov, P. Umari, R.M. Wentzcovitch, QUANTUM ESPRESSO: a modular and open-source software project for quantum simulations of materials, J. Phys. Condens. Matter 21 (39) (2009) 395502, https://doi.org/10.1088/0953-8984/21/39/395502.

[45] P. Giannozzi, O. Andreussi, T. Brumme, O. Bunau, M.B. Nardelli, M. Calandra, R. Car, C. Cavazzoni, D. Ceresoli, M. Cococcioni, N. Colonna, I. Carnimeo, A.D. Corso, S. de Gironcoli, P. Delugas, R.A. DiStasio, A. Ferretti, A. Floris, G. Fratesi, G. Fugallo, R. Gebauer, U. Gerstmann, F. Giustino, T. Gorni, J. Jia, M. Kawamura, H.-Y. Ko, A. Kokalj, E. Küçükbenli, M. Lazzeri, M. Marsili, N. Marzari, F. Mauri, N.L. Nguyen, H.-V. Nguyen, A.O. de-la Roza, L. Paulatto, S. Poncé, D. Rocca, R. Sabatini, B. Santra, M. Schlipf, A.P. Seitsonen, A. Smogunov, I. Timrov, T. Thonhauser, P. Umari, N. Vast, X. Wu, S. Baroni, Advanced capabilities for materials modelling with Quantum ESPRESSO, J. Phys. Condens. Matter 29 (46) (2017) 465901, https://doi.org/10.1088/1361-648x/aa8f79.

[46] K.F. Garrity, J.W. Bennett, K.M. Rabe, D. Vanderbilt, Pseudopotentials for high-throughput DFT calculations, Comput. Mater. Sci. 81 (2014) 446, https://doi.org/10.1016/j.commatsci.2013.08.053.

[47] M.B. Nielsen, D. Ceresoli, J.-E. Jørgensen, C. Prescher, V.B. Prakapenka, M. Bremholm, Experimental evidence for pressure-induced first order transition in cerium nitride from B1 to B10 structure type, J. Appl. Phys. 121 (2) (2017) 025903, https://doi.org/10.1063/1.4973575.

[48] J.P. Perdew, A. Ruzsinszky, G.I. Csonka, O.A. Vydrov, G.E. Scuseria, L.A. Constantin, X. Zhou, K. Burke, Restoring the density-gradient expansion for exchange in solids and surfaces, Phys. Rev. Lett. 100 (2008) 136406, https://doi.org/10.1103/PhysRevLett.100.136406.

[49] X. Shao, P. Liu, C. Franchini, Y. Xia, J. He, Assessing the performance of exchange-correlation functionals on lattice constants of binary solids at room temperature within the quasiharmonic approximation, Phys. Rev. B 108 (2) (2023), https://doi.org/10.1103/physrevb.108.024306.

[50] S. Baroni, S. de Gironcoli, A. DalCorso, P. Giannozzi, Phonons and related crystal properties from density-functional perturbation theory, Rev. Mod. Phys. 73 (2001) 515, https://doi.org/10.1103/RevModPhys.73.515.

[51] D. Errandonea, Landau theory applied to phase transitions in calcium orthotungstate and isostructural compounds, Europhys. Lett. (EPL) 77 (5) (2007) 56001, https://doi.org/10.1209/0295-5075/77/56001.

[52] G. Rogl, D. Legut, R. Sýkora, P. Müller, H. Müller, E. Bauer, S. Puchegger, M. Zehetbauer, P. Rogl, Mechanical properties of non-centrosymmetric CePt$_3$Si and CePt$_3$B, J. Phys. Condens. Matter 29 (18) (2017) 185402, https://doi.org/10.1088/1361-648x/aa655b.

[53] M. Nicklas, F. Steglich, J. Knolle, I. Eremin, R. Lackner, E. Bauer, Pair breaking by nonmagnetic impurities in the noncentrosymmetric superconductor CePt$_3$Si, Phys. Rev. B 81 (18) (2010) 180511, https://doi.org/10.1103/PhysRevB.81.180511.

[54] J. Zhu, H. Xu, J. Zhang, C. Jin, L. Wang, Y. Zhao, Thermal equations of state and phase relation of PbTiO$_3$: A high P-T synchrotron x-ray diffraction study, J. Appl. Phys. 110 (8) (2011) 084103, https://doi.org/10.1063/1.3651377.

[55] P. Pruzan, D. Gourdain, J.C. Chervin, B. Canny, B. Couzinet, M. Hanfland, Equation of state of BaTiO$_3$ and KNbO$_3$ at room temperature up to 30 GPa, Solid State Commun. 123 (1) (2002) 21, https://doi.org/10.1016/S0038-1098(02)00201-6.

[56] R.S. Kumar, A.L. Cornelius, M.F. Nicol, Equation of state of nanocrystalline BaTiO$_3$ up to 52 GPa at room temperature, Phys. Status Solidi B 244 (1) (2007) 290, https://doi.org/10.1002/pssb.200672572.